Particle Grinding by High-Intensity Ultrasound: Kinetic Modeling and Identification of Breakage Mechanisms

Vinay Raman
Dept. of Chemical Engineering, Indian Institute of Technology Madras, Chennai 600036, Tamilnadu, India

Ali Abbas
School of Chemical and Biomedical Engineering, Nanyang Technological University, 639798 Singapore, Singapore

School of Chemical and Biomolecular Engineering, The University of Sydney, Sydney, NSW 2006, Australia

Wenting Zhu
School of Chemical and Biomedical Engineering, Nanyang Technological University, 639798 Singapore, Singapore

DOI 10.1002/aic.12415
Published online September 24, 2010 in Wiley Online Library (wileyonlinelibrary.com).

High-intensity ultrasound, is sought as a means to break particles. A horn-type ultrasonic transducer is used to apply HIU into a suspension of alumina particles causing breakage to occur. The rate of particle breakage is monitored continuously via in-line laser-based particle chord length measurement. Kapur function analysis is used to arrive at the grinding kinetics under variations of ultrasonic power, particle loading, temperature of the suspension and particle size. The first Kapur function increases monotonically with increase in input ultrasonic power. Increasing temperature also increases the first Kapur function but an optimum in the range investigated (10–50°C) is observed near 25°C. An exponential relation is found for the variation of first Kapur function with particle size, this being unique to ultrasound-mediated particle breakage. The breakage mechanism is attributed mainly to particle abrasion. Different breakage mechanisms are observed at different temperatures. © 2010 American Institute of Chemical Engineers *AIChE J,* 57: 2025–2035, 2011
Keywords: ultrasound, grinding, particle breakage, FBRM, Kapur function

Introduction

Particle size reduction is a critical industrial operation relevant to a large sector of the chemical process industries. As far as the pharmaceutical, ceramic, minerals, and other industries are concerned, particles of specific size ranges are almost always targeted. In chemical reaction engineering, it is of great importance to prepare catalyst particles of suitable size with appropriate surface modifications. It has been a constant endeavor for many researchers to find new means for particle size reduction toward better efficiency, repeatability, and enhanced powder quality. The use of high-intensity ultrasound (HIU) for particle comminution is an attractive method that has many advantages, it is ideally suited for comminution of energetic materials,[1] it does not affect the thermal behavior of the sonicated materials,[2] and moreover, the introduction of impurities experienced in other size reduction methods (e.g., ball milling) is minimized in HIU operations, this being an advantage particularly for the pharmaceutical industry where purity of drugs is of major

Correspondence concerning this article should be addressed to A. Abbas at ali.abbas@sydney.edu.au.

concern. Furthermore, ultrasonically irradiated particles exhibit interesting surface modifications making them ideal for use as catalyst particles.

Particle breakage by HIU is caused by the erosion of particle surfaces because of the microjets emanating from asymmetric collapse of the transient cavitation bubbles.[3] Detailed studies addressing the effects of HIU variables on particle breakage characteristics are warranted. Such studies aid in the development of dynamic models that subsequently facilitate scale-up and process development. Breakage rate equations can be derived from experimental data and used to characterize the macroscopic performance of this system. This has been shown in previous studies, of traditional comminution methods, that established breakage kinetic functions.[4–6] Other workers more recently applied this technique to new grinding equipment successfully.[7]

In this study, we calculate the breakage and selection functions of the ultrasound-mediated particle breakage based on the simplified model used in previous works.[8–11] We also discuss the effect of sonication power, particle size, and temperature of the bulk fluid on the breakage parameters. This would be helpful industrially for scale-up purposes. Furthermore, the breakage mechanism is established based on the cumulative breakage distribution function. Two mechanisms of grinding are identified.[12] One is abrasion, which is the mechanism of size reduction, by which significantly smaller particles are chipped away from the edges and surfaces of the original particle resulting in bimodal size distributions. Another mechanism of fracture is the mechanism where the original particle is broken into variably sized smaller ones resulting in a broad distribution of sizes. Breakage and grinding are interchangeably used in this article synonymously referring to the collective effect of both fracture and abrasion mechanisms.

Calculation of Breakage Parameters

Breakage and selection functions are the characteristic descriptors of any grinding process and are used here to characterize ultrasound-mediated grinding. This is, as far as the authors are aware, the first such treatment using these functions in ultrasound-mediated particle grinding. The breakage function (b_{ij}) gives the distribution of fragments resulting from breakage of fraction of size x_j, whereas the selection function S_i is the rate constant for breakage of particles of size x_i. The change in particle size with time is governed by the differential equation

$$\frac{dm_i}{dt} = -S_i m_i(t) + \sum_{j=1}^{i-1} S_j b_{ij} m_j(t), \tag{1}$$

where m_i is the mass fraction of size class x_i at any time t. Converting Eq. 1 into cumulative form, we have

$$\frac{dR_i}{dt} = -S_i R_i(t) + \sum_{j=1}^{i-1} R_j(t)\left[S_{j+1}B_{ij+1} - S_j B_{ij}\right], \tag{2}$$

where R_i is the cumulative oversize fraction for size x_i, whereas $B_{ij} = \sum_{k=i+1}^{n} b_{kj}$ is the cumulative breakage function. This represents the probability of fragments from breakage of size x_j to have a size less than x_i.

The breakage rate parameters (S_i and B_{ij}) are calculated after[8–10] which is valid for short grinding times, whereas the variation of cumulative oversize fraction with time for batch grinding is written after Kapur[11] as

$$R(x,t) = R(x,0)\exp\left[\sum_{k=1}^{p} K^{(k)}(x)\frac{t^k}{k!}\right], \tag{3}$$

where $R(x,t)$ is the cumulative oversize fraction above size x at any instant of time t, and $R(x,0)$ is the corresponding cumulative oversize fraction at the start of breakage. The terms in brackets comprise what is known as the Kapur functions from which the approximate specific breakage rate function or selection function and the breakage distribution functions can be derived. At any time t, a residual ratio is defined as

$$f(x,t) = \frac{R(x,t)}{R(x,0)}, \tag{4}$$

which represents the fraction of particles that have not been broken yet, and this is used to characterize the breakage process similar to chemical reactions, where conversion or extent of reaction is used as the characteristic parameter.

For short grinding times, Eq. 3 can be reduced[8] to give

$$f(x,t) = \exp\left(K^{(1)}t\right). \tag{5}$$

Now, by plotting $\log\left(\frac{R(x,t)}{R(x,0)}\right)$ vs. t, the first Kapur function $K^{(1)}$ is obtained. From the first Kapur function, the approximate specific breakage rate and cumulative breakage function are calculated as

$$S_i = -K_i^{(1)} \tag{6}$$

$$B_{i,j} = \frac{K_i^{(1)}}{K_j^{(1)}}. \tag{7}$$

The coarsest size class is numbered 1, and the class numbering ascends toward the finest size class.

Once B_{ij} is determined, the curve $B_{ij} = f\left(\frac{x_i}{x_j}\right)$ can be used to determine the mechanism of breakage. In principle, the curve is expected to lie between the two extreme curves shown in Figure 1, suggesting that the actual mechanism in most situations is a combination of abrasion and fracture.

As seen in Figure 1, if the experimental curve of B_{ij} is nearer to the abrasion curve, then it would suggest that the dominant breakage mechanism is abrasion and vice versa. Thus, the experimentally obtained B_{ij} curves are used to establish the breakage mechanism. However, it is important to note that this is only a qualitative analysis, because fracture mechanisms can be identified accurately only by detailed mass-based analyses[8] unlike abrasion, which is primarily a surface mechanism. Nevertheless, we can still get a good idea of the breakage mechanisms from this study. Moreover, this analysis allows identification of change in the breakage mechanisms, in terms of relative importance of abrasion over fracture or vice versa, as a function of the operational parameters.

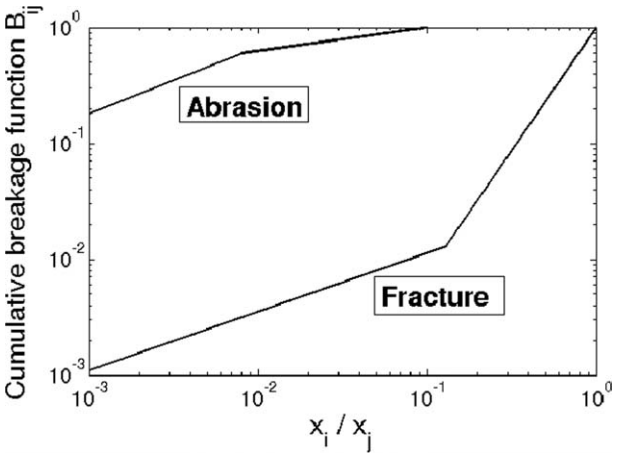

Figure 1. $B_{ij} = f\left(\frac{x_i}{x_j}\right)$ curves obtained for different mechanisms[13].

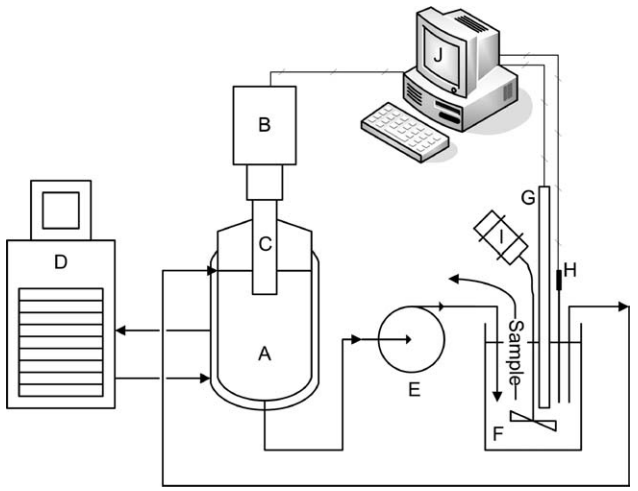

Figure 3. Experimental setup.

A: sonication vessel, B: frequency generator, C: ultrasonic transducer, D: temperature control, E: peristaltic pump, F: FBRM beaker, G: FBRM probe, H: temperature probe Pt100, I: agitator, and J: computer (data acquisition).

Experimental

Materials

Aluminum oxide (Al_2O_3) particles, insoluble in water, of mean size 150 μm were prepared by first grinding in a mortar standard-grade Al_2O_3 pellets before sieving using standard sieves (Advantec, Sonic Sifter). Figure 2 shows the ground particles used in the experiments as observed by SEM analysis.

As evident from Figure 2, the particles are relatively round (roundness index was found to be 0.72) with low aspect ratio. The surface texture looks primarily smooth; there are no dominant cleavage planes, suggesting that the breakage mechanism would preferably be abrasion rather than cleavage or fracture.

Equipment

The equipment, described previously in,[14] consists of a 24-kHz horn-type ultrasound transducer (Sartorius, Labsonic, Germany) capable of delivering a maximum of 450 W power. The ultrasonic transducer had a probe tip diameter of 22 mm and was operated at discrete amplitude ratios of 0.3, 0.5, and 0.7 corresponding to input powers of 150, 250, and 350 W, respectively. The horn depth was kept fixed at 3 cm below the air–water interface inside the jacketed glass flow reactor (sonication vessel), which had approximate internal dimensions of 4 cm internal diameter and 10 cm height. Temperature was measured using a Pt100 probe. The experimental setup shown in Figure 3 consisted of a variable speed peristaltic pump (Watson Marlow, USA), ultrasonic transducer, FBRM probe (Mettler-Toledo Lasentec Products, USA), temperature controller (Lauda, Germany), and a computer for continuous automatic data acquisition. Monitoring of particle size distribution (PSD) was achieved by drawing samples from the jacketed vessel and measuring, in-line, the chord length distribution (CLD) in a beaker using a FBRM probe. The peristaltic pump used for circulating the in-line flow was calibrated before use, and its flow rate was kept fixed at 1.6 l/min during all the experiments.

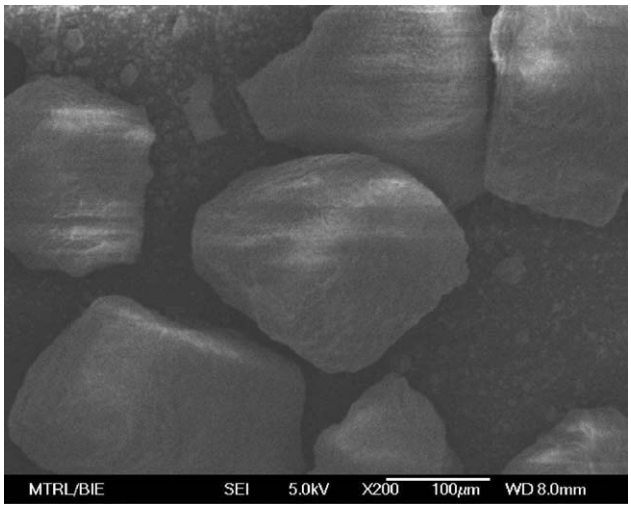

Figure 2. SEM micrograph of Al_2O_3 particles (before sonication) used in the batch experiment.

Methods

A summary of the experimental conditions is shown in Table 1. In a typical run, 2g of alumina particles was suspended in the vessel containing deionized water to which ultrasound was applied continuously for the duration of 10 min. The total volume of the suspension in the system was 750 ml. The particle size in the form of mean chord length (ℓ_m) was monitored in-line using the FBRM probe for the full duration of the experiment. The probe was inserted in the FBRM beaker that had flow from and to the sonication vessel. Such monitoring in the in-line mode was necessary first because the sonication vessel cannot accommodate the FBRM probe and second because it was necessary to keep the FBRM probe at a safe distance from the intense ultrasound field. The particle suspension was pumped from the sonication vessel (A) to the FBRM beaker (F) and circulated back to the sonication vessel (A) at a constant volumetric flow rate 1.6 l/min. Agitation in the FBRM beaker was kept fixed at 400 rpm. The agitator in the FBRM beaker had negligible effect on the particle breakage as tested by

Table 1. Details of Experimental Conditions

Exp. No.	Amplitude Ratio	Rated Input Power (W)	Temperature (°C)	Particle	Roundness Index
1	0.3	150	10 ± 3	Al_2O_3 (ground)	0.72
2	0.3	150	17 ± 2	Al_2O_3 (ground)	0.72
3	0.3	150	25 ± 2	Al_2O_3 (ground)	0.72
4	0.3	150	37 ± 1	Al_2O_3 (ground)	0.72
5	0.3	150	50 ± 1	Al_2O_3 (ground)	0.72
6	0.5	250	10 ± 2	Al_2O_3 (ground)	0.72
7	0.5	250	17 ± 1	Al_2O_3 (ground)	0.72
8	0.5	250	25 ± 2	Al_2O_3 (ground)	0.72
9	0.5	250	37 ± 1	Al_2O_3 (ground)	0.72
10	0.5	250	50 ± 1	Al_2O_3 (ground)	0.72
11	0.7	350	10 ± 3	Al_2O_3 (ground)	0.72
12	0.7	350	17 ± 2	Al_2O_3 (ground)	0.72
13	0.7	350	25 ± 1	Al_2O_3 (ground)	0.72
14	0.7	350	37 ± 1	Al_2O_3 (ground)	0.72
15	0.7	350	50 ± 1	Al_2O_3 (ground)	0.72
16	0.7	350	25 ± 2	Al_2O_3 (standard)	0.78
17	0.7	350	25 ± 1	Al_2O_3 (standard)	0.87

monitoring the mean size of the particles under agitation over a long period of time. A similar test was performed confirming the negligible effect of the peristaltic pump on particle breakage. The sonication and hence the run was started after a period of pumping that allowed the particles to suspend throughout the flow homogenously. FBRM particle size data and ultrasound transducer data were collected using two separate computers. The temperature probe was also connected to the computer recording temperature continuously. At the end of the run, a sample was withdrawn, isokinetically from the FBRM beaker using a plastic pipette, for microscopic analysis, which was carried out using field emission scanning electron microscope (JOEL, JSM6700F, Japan).

Particle size measurement

Focused beam reflectance method is an in situ method for determining the CLD of a suspension with low to high solids concentration.[15] A focused monochromatic infrared laser beam rotates at a fixed high speed, and the backscattered/reflected light signals from the surfaces of thousands of particles intersected by the laser light are captured. The time interval (Δt) between signals from the two edges of a particle is converted to chord length (s) by:

$$s = v_b * \Delta t, \tag{8}$$

where v_b is beam velocity. Because tens of thousands of such chord lengths are measured each second, a statistically representative CLD of the particle system under investigation is generated. Figure 4 illustrates the measurement technique.

The FBRM is a well-established technique that has been used to monitor size distributions in crystallization[16–18] as well as in biotechnology[19,20] amongst other applications. Kovalsky and Bushell[21] used this technique for on-line characterization of floc size and structure. They used Fourier transform of the unprocessed signal (i.e., the reflected signal) to arrive at the mass fractal dimensions of the flocs. It is also claimed that apart from size and shape, the unprocessed reflected signals could also yield information on particle texture. Throughout this work, we characterized particle size and hence breakage by HIU in terms of chord lengths. Therefore, the use of the word "size" throughout this work refers to sizing data obtained through chord length measurements. The motivation for this lies in the reliability of the measurement technique as well as in the fact that decreasing chord length is a direct indication of fragmentation. Several studies developed mathematical relationships and correlations between CLD and PSD and have shown restoration of PSD from CLD data.[22–25] FBRM generates number counts of particles that are weighted by their chord lengths, because the probability of detection of the particle by the probe is directly proportional to its diameter or chord length. The volume fraction for the different size classes of the particles is obtained by square weighting the number counts with chord lengths.[26] It has been shown in Ref. 26 that there is a very good agreement of the FBRM CLD data, for alumina particles (size range 20–200 μm), with the PSD data from other sizing methods like laser diffraction when square weighting by chord length is performed for raw FBRM CLD data. Hence, we adopted the methodology of Ref. 26 to

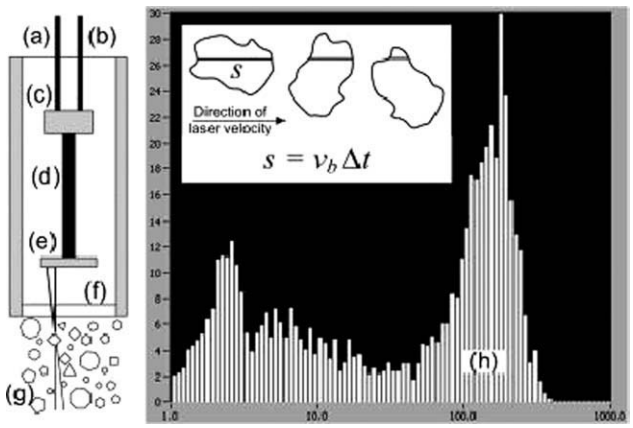

Figure 4. Particle size measurement using FBRM.

(A) Laser diode, (B) detector, (C) beam splitter, (D) laser beam, (E) optics rotating at fixed high velocity, (F) sapphire window, (G) particles, and (H) typical chord length distribution.

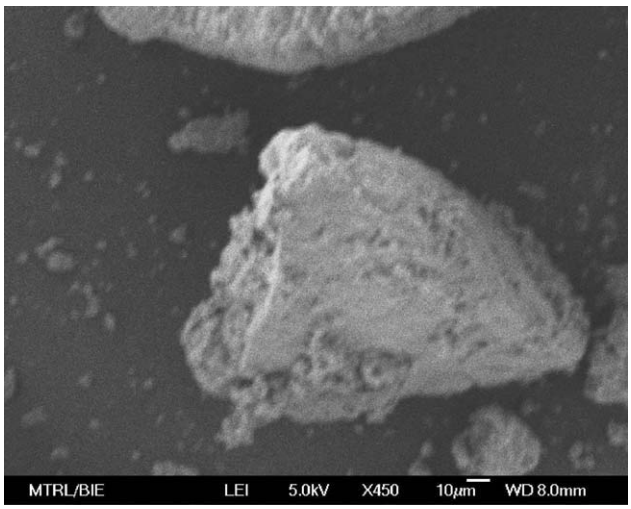

Figure 5. Effect of ultrasound on the surface morphology of the particles.

obtain the cumulative oversize fractions for various particle size classes on which the Kapur function model is based.

Results and Discussion

A steady decrease in the square-weighted mean chord length ℓ_m was observed with time after the induction of ultrasound.[14] The SEM micrographs revealed pitting and surface erosion of the particles (Figures 5 and 6). Such modification to the particle surface can lead to enhanced reaction activity when such particles are used for catalysis.

Calculation of first Kapur function

The FBRM probe is configured to give the time-varying data for the cumulative undersize fraction of sizes ranging from 1 to 1000 μm in 90 log channels. From these channels, 10 particle size classes were chosen (Table 2) and extracted for doing the calculations. The numbering of these classes,

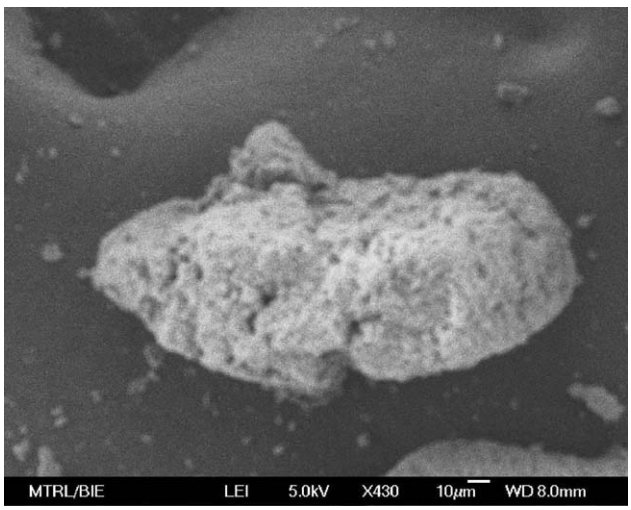

Figure 6. Effect of ultrasound on the surface morphology of the particles.

Table 2. Definition of Particle Size Classes

Particle Class *i,j*	Particle Size Range (μm)
1	> 171.133
2	116.591–171.133
3	79.433–116.591
4	54.117–79.433
5	36.869–54.117
6	25.119–36.869
7	17.113–25.119
8	11.659–17.113
9	7.943–11.659
10	5.412–7.943

as mentioned, is done in the reverse order, where 10 refers to finest size 5.412 and 1 refers to coarsest size 171.133. The cumulative undersize fraction curves were converted to cumulative oversize fraction curves before calculating the residual ratios for the 10 sizes chosen. The residuals are calculated in this way for a time interval of 45 s. Figure 7 shows the variation of the residual ratio with time for amplitude ratio of 0.7 at a temperature of 25°C.

The sonication was started only after a stable signal from the FBRM probe was sustained. This is evident from the first 400 s in Figure 7. The breakage occurs immediately once the sonication starts and is reflected by the decrease of cumulative oversize fraction for all sizes, consequently the residual ratio decreases with sonication time. Similar variation was obtained for other amplitude ratios and at other temperatures (Figure 8).

For every size class, a linear decrease in $\ln(f(x,t))$ was observed with time. We obtain the first Kapur function from the slopes of the $\ln(f(x,t))$-time plots at the first 45 s. A representative plot is shown in Figure 9 for the size class 36.869–54.117 μm at amplitude ratio and temperature of 0.7 and 25°C respectively. Similar plots were obtained for all the size classes for all the experiments conducted, and the Kapur functions were calculated for different amplitude ratios and temperatures. Good fits were obtained with all correlation coefficients, R^2, exceeding 0.95.

Dependence on ultrasonic power

Three different ultrasound power levels were used for the experiment, namely, 150, 250, and 350 W corresponding to

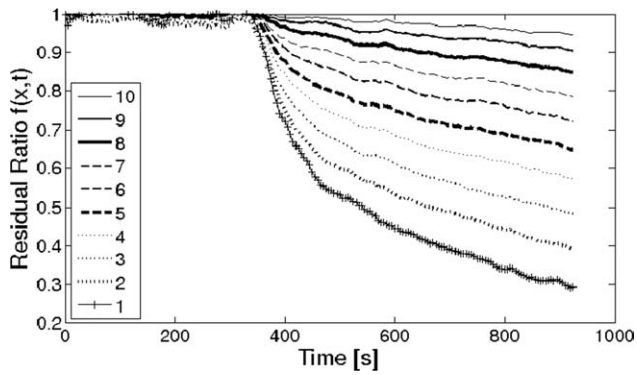

Figure 7. Variation of residual fraction with time for different sizes, amplitude ratio = 0.7 and temperature = 25°C.

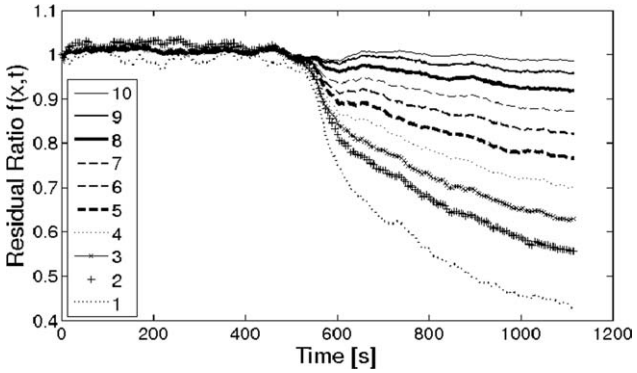

Figure 8. Variation of residual ratio with time, amplitude ratio = 0.5 and temperature = 25°C.

the amplitude ratios of 0.3, 0.5, and 0.7, respectively. Figure 10 shows the variation of first Kapur function with size for different amplitude ratios. The absolute magnitude of the first Kapur function for all the sizes increased with increase in input power. From the first Kapur function, the selection functions for all the sizes were calculated using Eq. 6.

The increase in the magnitude of first Kapur function with increasing input power suggests that higher breakage can be achieved by increasing the ultrasound intensity or input ultrasonic power. Creating new surfaces is an energy-intensive process. At higher input power, more energy is available for breakage. This is well illustrated in Figure 11, which shows the variation of mean chord length ratio (MCLR) of broken particles with total input energy as measured by an in-built watt meter in the ultrasound equipment. We define the dimensionless number MCLR as

$$\mathrm{MCLR}(t) = \frac{\ell_{\mathrm{m}}(t)}{\ell_o}, \tag{9}$$

where ℓ_o is the initial mean chord length in micron. For a constant sonication time of 10 min and by operating at a higher amplitude ratio of 0.7, more energy is input to the system. This is reflected in the percentage decrease in MCLR at the end of 10 min, which is higher for amplitude ratio of 0.7 than it is for

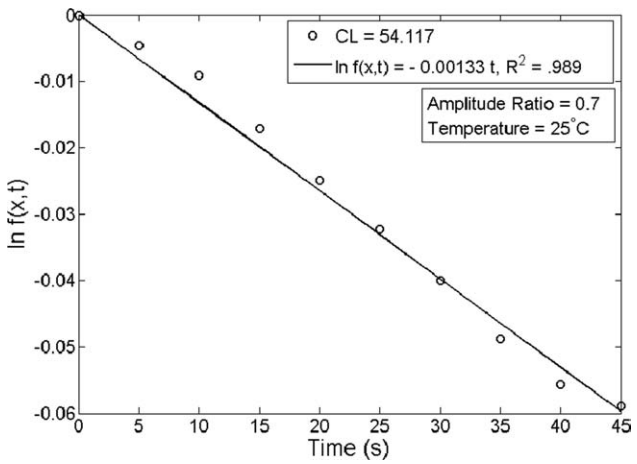

Figure 9. Calculation of first Kapur functions for the selected chord length.

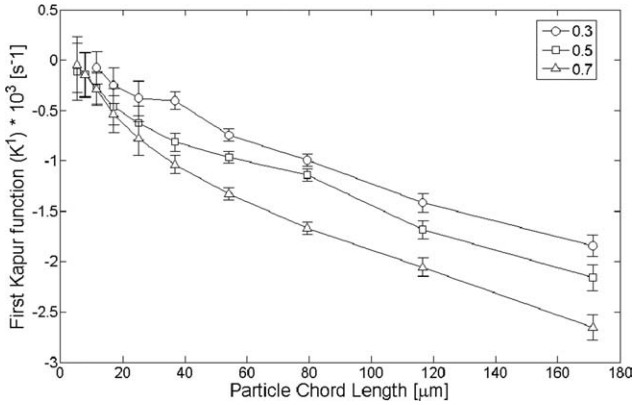

Figure 10. Variation of first Kapur function with size at different amplitude ratios.

0.5 and 0.3. In other words, higher energy input to the system results in higher breakage, which is true for any comminution process and is here verified for ultrasound-mediated particle breakage as well.

Furthermore, larger selection functions are obtained for larger sizes, which is consistent with the fact that bigger particles are easier to break than smaller ones. This confirms that particle breakage is dependent on particle size. Attainment of larger selection functions at higher amplitude ratios can be checked by the temporal variation of MCLR for different amplitude ratios shown in Figure 12.

It is evident from Figure 12 that higher amplitude ratios result in higher breakage following the same trend of the selection function change with amplitude ratio. Highest percentage decrease in MCLR is obtained for an amplitude ratio of 0.7, which is about 15%.

Dependence on temperature

Five different experiments were conducted each at one temperature in the range of 10–50°C, at a constant flow rate of 1600 ml min, and each was repeated at all the three amplitude ratios of 0.3, 0.5, and 0.7. The first Kapur functions were calculated for all the 10 selected sizes for all these experiments. Figure 13 shows the variation of first Kapur function with temperature for different size classes when the system is operated at a constant amplitude ratio of 0.7.

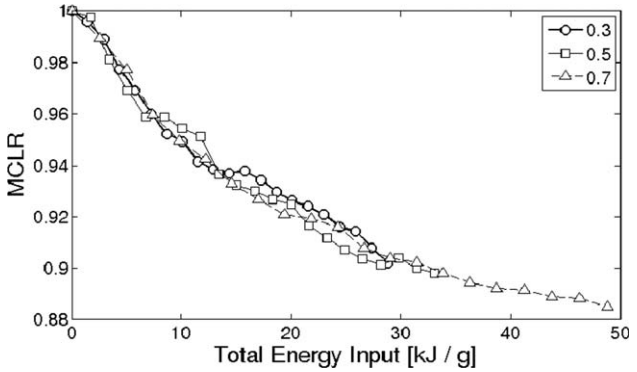

Figure 11. Variation of MCLR with total energy, sonication time = 10 min and temperature = 25°C.

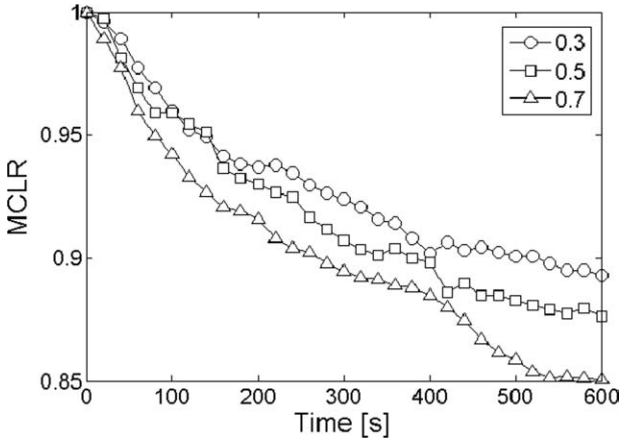

Figure 12. Variation of MCLR vs. time for different amplitude ratios at 25°C.

The magnitude of the first Kapur function initially shows an increase with temperature and then decreases after some optimum temperature. This trend was seen mainly for the larger particles (size class 1, 2, and 3), whereas for the smaller particles there was almost no variation. For the larger size classes (1, 2, and 3), this optimum temperature was found to be 25°C. This suggests that the breakage is the highest at a temperature near 25°C when operating the system at a constant amplitude ratio of 0.7. This is consistent with the temporal variation of MCLR for different temperatures as shown in Figure 14.

From Figure 14, we observe that for 10 min of sonication at an amplitude ratio of 0.7, the highest breakage is obtained when operated at a bulk fluid temperature of 25°C. Figure 15 shows the percentage decrease in MCLR of the particles at the end of 10 min of sonication for different temperatures of operation for three different amplitude ratios of 0.3, 0.5, and 0.7. From this data, temperature is seen to have a significant effect on the cavitation phenomenon and is explained as follows.

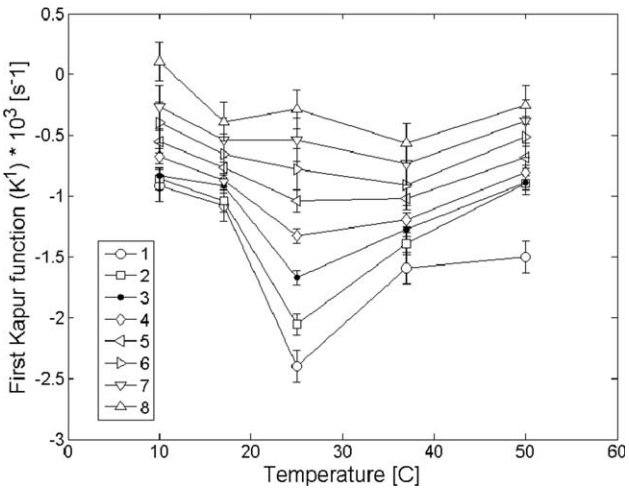

Figure 13. Variation of first Kapur function with temperature for different particle sizes.

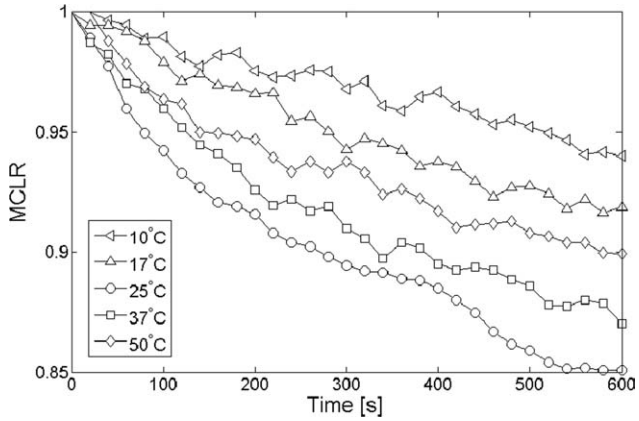

Figure 14. Variation of MCLR vs. time at different temperatures and at amplitude ratio of 0.7.

The cavitation phenomenon in a liquid medium is affected by its surface tension, viscosity, and vapor pressure.[27,28] Increasing temperature results in reduction in acoustic cavitation threshold, meaning the liquids cavitate at lower intensities.[28] This can be attributed to the increase in vapor pressure of the liquid when temperature is raised. The increase in temperature results in decrease in surface tension, again aiding in the reduction of the cavitation threshold. Moreover, increasing the temperature reduces the viscosity of the liquid medium. The decrease in viscosity decreases the magnitude of the natural cohesive forces acting on the liquid and thus decreases the magnitude of the cavitation threshold. Lower cavitation thresholds translate into ease of cavity formation, thereby making higher temperatures more favorable for particle breakage. Thus, the effect of temperature constitutes three mechanisms that all lead to enhanced cavitation inception, which in turn enhance the breakage. This discussion assumes that it is the high-speed microjets emanating from the asymmetric transient cavitation collapse that cause the breakage.[3] This is the reason why we observe an increase in breakage of particles as temperature is varied from 10 to 25° C. As temperature is increased beyond 25°C, we observe a decrease contradicting the current discussion on the

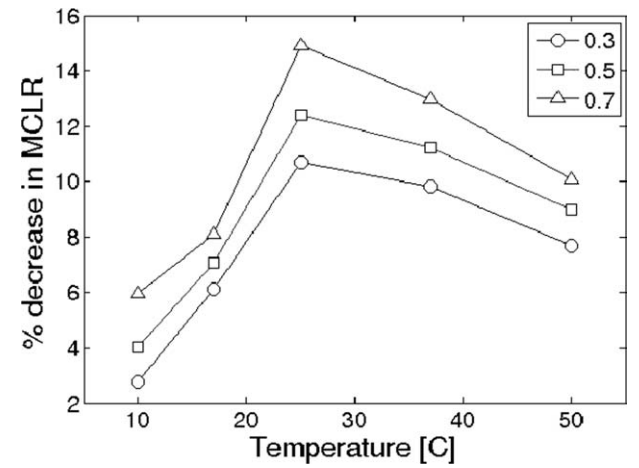

Figure 15. Percentage decrease in MCLR for different temperatures and amplitude ratios.

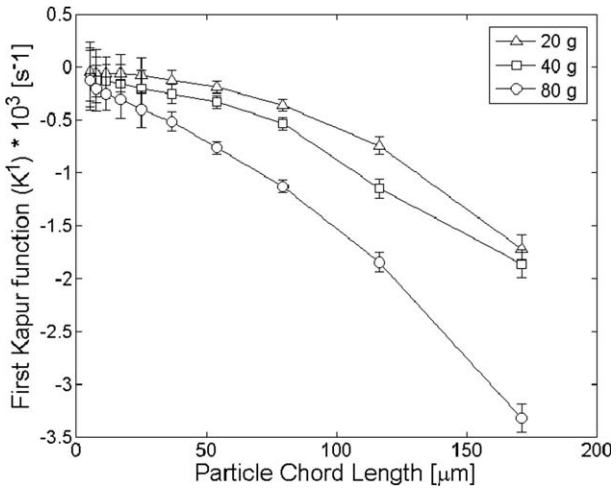

Figure 16. Variation of first Kapur function with size at different particulate loading levels, amplitude ratio = 0.7 and temperature = 25°C.

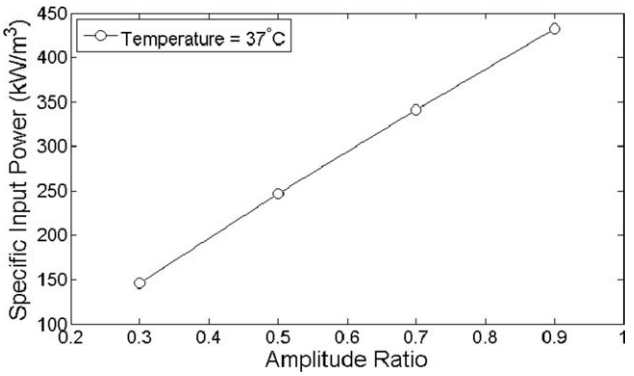

Figure 17. Variation of input specific power with amplitude ratio at 37°C.

temperature effect. This can be explained as being primarily caused by the cushioning effect of increased cavity internal vapor pressure at higher temperatures.[28] Because of this cushioning effect, the intensity of the collapse and subsequently the breakage decreases after 25°C. There are thus two opposing factors that are at play during the particle breakage; first, the increase in the number of cavitation events with increase in temperature and because of which particle breakage increases, and second, the cushioning effect of the cavity internal vapor pressure, which has a suppression effect on the cavitation intensity and subsequently on particle breakage. It is the relative magnitude of these two opposing effects that dictates the variation of breakage characteristics with temperature as seen in Figure 15. The former factor is dominant in regions of temperature near and below 25°C whereas the latter becomes more dominant as temperature moves above 25°C.

This is consistent with the variation of cavitation erosion with temperature observed elsewhere.[29–32] This suggests that two temperature-dependent factors are important as far as the particle breakage is considered, namely, the size of active cavitation zone and the effect of vapor pressure. The former increases with increase in temperature and has a positive effect, whereas the latter has a negative effect. Thus, the breakage shows a maximum at 25°C as observed in the temperature variation of MCLR (Figure 15).

Dependence on particle loading

Figure 16 shows the variation of first Kapur function with particle size for different particulate loading levels of 20, 40, and 80 g. It is evident that higher breakage is observed at higher particulate loading levels, which can be attributed to higher rate of interparticle collisions. The probability of collision becomes higher at higher loading levels.

Model for ultrasound-mediated particle breakage

We would like to be able to predict ultrasound-mediated particle breakage. With this aim, we discuss here the development of the breakage model stemming from the experimental analysis discussed in the previous sections.

The variation of residual ratio with time for short grinding times can be written as

$$f(x,t) = \exp\left(K^{(1)}(x)t\right). \tag{10}$$

In the previous sections, we learnt that the first Kapur function is dependent on amplitude ratio, particle size,

Table 3. Correlation Coefficients for the First Kapur Function

Exp. No.	Amplitude Ratio	Rated Power (W)	Temperature (°C)	a_o *10^3 (s^{-1})	a_1 *10^3 (s^{-1})	b (s^{-1})	R^2 (μm^{-1})
1	0.3	150	10	0.5302	0.6711	0.0197	0.982
2	0.3	150	17	0.5057	0.6539	0.9635	0.985
3	0.3	150	25	1.9693	1.6785	0.01	0.992
4	0.3	150	37	0.8311	0.8817	0.0366	0.969
5	0.3	150	50	0.6087	0.7261	0.02168	0.97
6	0.5	250	10	0.5302	0.6711	0.0197	0.971
7	0.5	250	17	0.5057	0.6539	0.9635	0.991
8	0.5	250	25	1.9693	1.6785	0.01	0.979
9	0.5	250	37	0.8311	0.8817	0.0366	0.981
10	0.5	250	50	0.6087	0.7261	0.02168	0.976
11	0.7	350	10	0.5302	0.6711	0.0197	0.988
12	0.7	350	17	0.5057	0.6539	0.045	0.9845
13	0.7	350	25	1.9693	1.6785	0.01	0.995
14	0.7	350	17	0.8311	0.8818	0.0366	0.972
15	0.7	350	50	0.6088	0.7261	0.02168	0.971

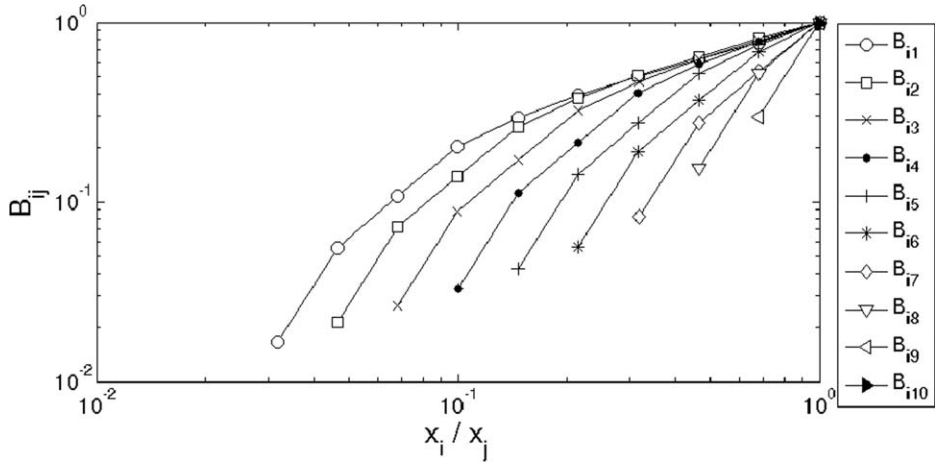

Figure 18. $B_{i1} = f\left(\frac{x_i}{x_1}\right)$ curves for different sizes, amplitude ratio = 0.5 and temperature = 25°C.

temperature, and particle load. Other researchers have modeled the first Kapur function as a power law function of size.[7,9,10] We propose a new exponential-structured formulation for the first Kapur function taking into account dependence not only on particle size as previously presented[7,9,10] but to also include other operational parameters, in this case amplitude ratio (specific to ultrasound processes) and temperature. This extension is unique to this work and to ultrasound-mediated particle breakage. Although it is possible to extend the formulation to account for the dependence on particle loading, we refrain from doing so for the purpose of model brevity. The proposed first Kapur function formulation is written as

$$K^{(1)}(x) = -a\left(1 - e^{-bx}\right). \tag{11}$$

The coefficient a is identified to be a function of amplitude ratio at a given temperature and is given by

$$a = a_o + a_1 \frac{\xi}{\xi_{\max}}, \tag{12}$$

where $\frac{\xi}{\xi_{\max}}$ is the amplitude ratio, which has direct and linear relationship with the amount of input ultrasonic power. Such relationship is shown in Figure 17, where the specific input power refers to the calorimetrically measured power per unit volume.[33]

The final model is thus written as

$$K^{(1)}(x) = -\left(a_o + a_1 \frac{\xi}{\xi_{\max}}\right)\left(1 - e^{-bx}\right). \tag{13}$$

The coefficients a_o, a_1, and b for the different experimental conditions were obtained by linear least square regression. Their values are listed in Table 3.

Breakage mechanism

The cumulative breakage distribution function (B_{ij}) is calculated from the first Kapur function for different conditions of operation using Eq. 7. B_{ij} is plotted against $\frac{x_i}{x_j}$ (Figure 18) and a comparison is made against the abrasion and fracture cases in relation to Figure 1.[12,13]

Figure 18 indicates that larger particles undergo abrasion, whereas the smaller ones primarily undergo fracture. This can primarily be attributed to increase in energy requirement to fragment smaller particles. Because abrasion is caused by low-intensity surface stresses that are localized, it is a less effective breakage mechanism for smaller particles.

Figure 19 shows the fragments size distribution of larger particles, $B_{i1} = f\left(\frac{x_i}{x_1}\right)$ curves for different input amplitude ratios at a constant temperature of 25°C. It is shown that at 25°C and in relation to Figure 1, abrasion is the major breakage mechanism irrespective of the input ultrasonic power. Moreover, there is a big shift in the curve toward the abrasion region when the input ultrasonic power is changed from 150 to 250 W. Further increase in input ultrasonic power results in relatively less shift in the curve further toward the abrasion region. This suggests that, with increase in input ultrasonic power, abrasion becomes the more dominant breakage mechanism. At this point it is not very clear as to why abrasion is more favored at higher input ultrasonic power, but we speculate that this is attributable to the presence of larger cavitation zones.

Figure 20 shows the $B_{i1} = f\left(\frac{x_i}{x_1}\right)$ curves for different temperatures at a constant amplitude ratio of 0.7. The breakage

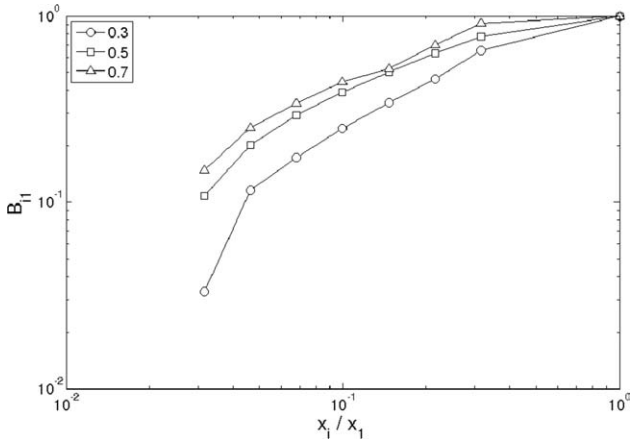

Figure 19. $B_{i1} = f\left(\frac{x_i}{x_1}\right)$ curves for different amplitude ratios at 25°C.

mechanism is observed to change with temperature. It shifts toward abrasion as temperature is increased. This can be attributed to increase in cavitation zone with increase in temperature as discussed in Section ''Dependence on Temperature''. An increased number of transient cavitation events occurs at higher temperature, which are capable of causing abrasion but not fracture because of lower intensity of impact caused by cushioning effect of increased vapor pressure at higher temperature. At low temperatures and even though the cavitation zone is smaller, the intensity of collapse of acoustic bubble is higher. The microjets created by such highly intense collapsing bubble are capable of causing particle breakage by fracture.

There is not much difference between the breakage mechanism at 10 and at 17°C while both being closer to the fracture region and similarly, little difference exists between 37 and 50°C, though this time both the latter are closer to the abrasion region. There is a relatively large shift in the breakage mechanism from 17 to 25°C and another similar shift from 25 up to 37°C. Optimal temperature for breakage was determined to be near 25°C, which along with the data presented here in Figure 20 suggests that a combination of abrasion and fracture results in higher breakage rather than having the breakage being dominated by any one mechanism.

The effect of loading on the breakage mechanism is shown in Figure 21 at a constant temperature of 25°C and an amplitude ratio of 0.7. A higher particulate load favors fracture, which can be attributed to increased interparticle impacts that are instrumental in particle breakage that is dominated by the fracture mechanism.

Conclusions

The kinetics of ultrasound-mediated particle breakage was modeled based on the Kapur function approach and via rigorous experimentation. We modeled the variation of first Kapur function with mean particle size under varying magnitudes of manipulated variables of the ultrasonic system, namely, amplitude ratio and temperature. The variation of first Kapur function with amplitude ratio and with temperature was explained as the effect of the latter variables on the cavitation erosion phenomenon responsible for the particle breakage. The breakage mechanism was deduced from the calculated cumulative breakage functions. Abrasion was found to be the dominant breakage mechanism; however, fracture was also found to occur for specific cases. The breakage mechanism was found to be significantly affected by amplitude ratio and temperature, a finding that is unique to ultrasound-mediated particle breakage. As far as the authors are aware, this is the first time that the mechanism of ultrasound-mediated particle breakage is quantified in this way and conferred. The nature of interparticle collisions is yet to be determined to delineate the role such collisions play. Further studies, involving temporal monitoring of selection functions and breakage mechanisms, are warranted to gather further understanding on ultrasound-mediated particle breakage. Such understanding will be of interest to industrialists looking for design, scale-up, and operation of ultrasound grinding equipment. Further work looking at the repeatable production of catalyst particles prepared in this way is called for. The modeling approach, based on Kapur functions, used in this study is valid only for short sonication times and gives only a qualitative picture of the breakage mechanisms involved. At longer sonication times, there could be other phenomena at play like variation of cavitation zones within the sonication vessel because of increase in the number of particles with breakage, or internal classification of the particles resulting in removal of fines from active cavitation zones to dead zones within the vessel, etc.

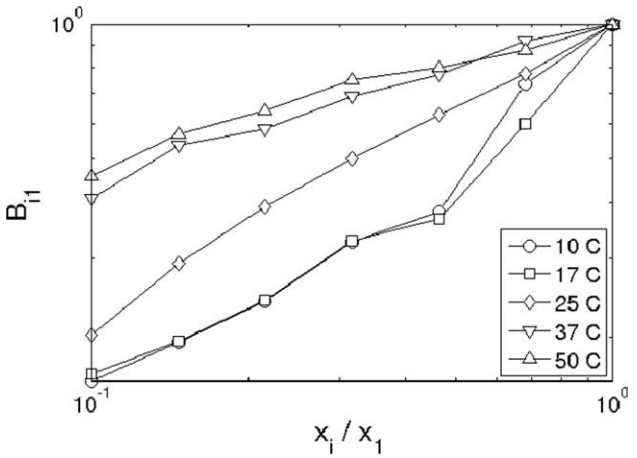

Figure 20. $B_{i1} = f\left(\frac{x_i}{x_1}\right)$ curves for different temperatures, amplitude ratio = 0.7.

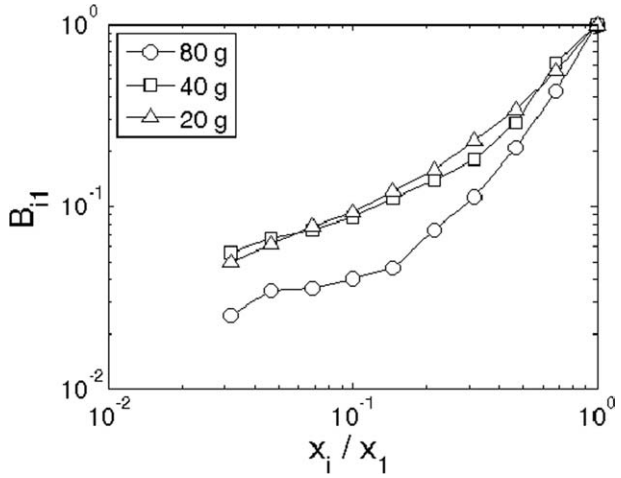

Figure 21. $B_{i1} = f\left(\frac{x_i}{x_1}\right)$ curves for different particulate loading levels, amplitude ratio = 0.7 and temperature = 25°C.

Literature Cited

1. Teipel U, Leisinger K, Mikonsaari I. Comminution of crystalline material by ultrasonics. *Int J Miner Proces*. 2004;74S:S183–S190.
2. Perez-Maqueda L, Duran A, Perez-Rodriguez J. Preparation of submicron talc particles by sonication. *Appl Clay Sci*. 2005;28:245–255.
3. Suslick K, Casadonte D, Greent M, Thompson M. Effects of high intensity ultrasound on inorganic solids. *Ultrasonics*. 1987;25:56–59.
4. Epstein B. Logarithmico-normal distribution in breakage of solids. *Ind Eng Chem* 1948;40:2289–2291.
5. Reid KJ. A solution to batch grinding equation. *Chem Eng Sci*. 1965;20:953.

6. Austin LG. Introduction to the mathematical description of grinding as a rate process. *Powder Technol*. 1971;5:1.
7. Fukunaka T, Golmanb B, Shinohara K. Batch grinding kinetics of ethenzamide particles by fluidized-bed jet-milling. *Int J Pharm*. 2006;311;89–96.
8. Berthiaux H, Dodds J. Approximate calculation of breakage parameter from batch grinding tests. *Chem Eng Sci*. 1996;51:4509–4516.
9. Berthiaux H, Dodds J. Modeling fine grinding in a fluidized bed opposed jet mill. I. Batch grinding kinetics. *Powder Technol*. 1999;106:78–87.
10. Berthiaux H, Chiron C, Dodds J. Modeling fine grinding in a fluidized bed opposed jet mill. II. Continuous grinding. *Powder Technol*. 1999;106:88–97.
11. Kapur PC. Kinetics of batch grinding, Part b: an approximate solution to the grinding equation. *Trans Soc Miner Eng, AIME*. 1970;247:309–313.
12. Varinot C, Hiltgun S, Pons M-N, Dodds J. Identification of the fragmentation mechanisms in wet-phase fine grinding in a stirred bead mill. *Chem Eng Sci*. 1997;52:3605–3612.
13. Menacho JM. Some solutions for kinetics of combined fracture and abrasion breakage. *Powder Technol*. 1986;49:86–87.
14. Raman V, Abbas A. Experimental investigations on ultrasound mediated particle breakage. *Ultrason Sonochem*. 2008;15:55–64.
15. Worlitschek J. Monitoring, modeling and optimization of batch cooling crystallisation. Ph.D. thesis, Swiss Federal Institute of Technology, Zurich, 2003.
16. Schirg P, Wissler P. Membrane processes for the chemical and pharmaceutical industry and optimization of particulate processes by lasentec fbrm. *Chimia*. 2000;54:207–210.
17. Barrett P, Glennon B. In-line monitoring of crystal growth in batch crystllization operations. In: *Proceedings of the 14th International Symposium on Industrial Crystallization*, Cambridge, 1999:12–16.
18. Monnier O, Fevotte G, Hoff C, Klein JP. Model identification of batch cooling crystallizations through calorimetry and image analysis. *Chem Eng Sci*. 1997;52:1125–1139.
19. McDonald KA, Jackman AP, Hurst S. Characterization of plant suspension cultures using the focused beam reflectance technique. *Biotechnol Lett*. 2001;23:317–324.
20. Barrett P, Glennon B. In-line fbrm monitoring of particle size in dilute agitated suspensions. *Part Syst Charact*. 1999;16:207–211.
21. Kovalsky P, Bushell G. In situ measurement of fractal dimension using focussed beam reflectance measurement. *Chem Eng J*. 2005;111:181–188.
22. Wynn E. Relationship between particle-size and chord-length distributions in focused beam reflectance measurement: stability of direct inversion and weighting. *Powder Technol*. 2003;133:125–133.
23. Worlitscheck MMJ, Hocker T. Restoration of PSD from chord length distribution data using the method of projections on to convex sets. *Part Part Syst Charact*. 2005;22:81–98.
24. Vaccaro MMA, Šefčik J. Modeling focused beam reflectance measurement and its application to sizing of particles of variable shape. *Part Part Syst Charact*. 2006;23:360–373.
25. Ehrl MML, Soos M. Sizing polydisperse dispersions by focused beam reflectance and small angle static light scattering. *Part Part Syst Charact*. 2006;23:438–447.
26. Heath AR, Fawell PD, Bahri PA, Swift JD. Estimating average particle size by focussed beam reflectance measurement (fbrm). *Part Part Syst Charact*. 2002;19:84–95.
27. Thompson L, Doraiswamy L. Sonochemistry: science and engineering. *Ind Eng Chem Res*. 1999;38:1215–1249.
28. Mason T, Lorimer J. *Applied Sonochemistry: The Uses of Power Ultrasound in Chemistry and Processing*. Weinheim: Wiley - VCH Verlag GmbH & Co. KGaA, 2002.
29. Plesset M. Temperature effects in cavitation damage. *Trans ASME J Basic Eng*. 1972;94:559–566.
30. Hattori S, Tanaka Y. Influence of air content and vapor pressure of liquids on cavitation erosion. *Trans JSME*. 2002;68 B:130–136.
31. Hattoria S, Gotoa Y, Fukuyama T. Influence of temperature on erosion by a cavitating liquid jet. *Wear*. 2006;260:1217–1223.
32. Kwok C, Man H, Leung L. Effect of temperature, pH and sulphide on the cavitation erosion behaviour of super duplex stainless steel. *Wear*. 1997;211:84–93.
33. Ratoarinoro F, Contamine A, Wilhelm J, Berlan H, Delmas H. Power measurement in sonochemistry. *Ultrason Sonochem*. 1995;2:S43–S47.

Manuscript received Feb. 21, 2010, revision received Jun. 14, 2010, and final revision received Aug. 18, 2010.